Progress In Electromagnetics Research, PIER 23, 1–38, 1999

SCATTERING FROM A THIN WIRE EXCITED BY A PERPENDICULAR LINE CURRENT

M. M. Sheikh and D. G. Dudley

ECE, Bldg. 104
University of Arizona
Tucson, AZ 85721, USA

1. Introduction
2. Formulation
3. Features of Complex Planes
4. Asymptotic Analysis
5. Dipole Source Excitation
6. Numerical Results
7. Conclusion
Appendices
References

1. INTRODUCTION

In this paper, we study the coupling from a line current source to a nearby wire. In our application, the source and the wire are perpendicular to each other.

The analysis of coupling to wires from dipoles or other wires is relatively recent. In a paper appearing in 1977 [1], the authors used full-wave scattering techniques to formulate the current induced on a horizontal wire above earth by a vertical electric dipole (VED), and obtained approximate solutions when the VED is electrically distant. In the same year, Hill and Wait [2] investigated coupling between an arbitrarily oriented electric or magnetic dipole and a horizontal cable over an ideal ground. They presented results for far field radiation and modal currents of a leaky coaxial cable excited by a VED. In a series of two consecutive papers, Wait investigated the excitation

of a coaxial cable above ground by a VED [3] and the excitation of an ensemble of parallel horizontal lines above a layered ground by a similar source [4]. No numerical results were presented in either paper. Later, the emphasis shifted to coupling between crossing conductors on microstrip and microwave circuits where one or both conductors may carry incident currents. Giri *et al.* [5] developed an equivalent circuit approximate model for the junction of two skewed transmission lines, where the inductive coupling was solved in close form and the capacitances obtained by solving coupled integral equations. In that paper the authors assumed TEM propagation on both conductors.

Different approaches were followed by other authors to develop similar coupling models: Kami and Sato [6] used transmission line theory and assumed that the power returning to the exciting line is negligible. Uwano *et al.* [7] analyzed crossing strip lines on a suspended substrate using a generalized transverse resonance technique. Papatheodorou *et al.* [8] used the method of moments to solve coupled integral equations derived for a microstrip crossover in a dielectric substrate backed by a ground plane. Young [9] developed a closed form approximation for TEM capacitive coupling between orthogonally crossing wires over a ground plane using full-wave scattering analysis. Finally, in a recent paper, Wait [10] presented a self-contained canonical solution for the currents excited on an overhead cable by a vertical line of current of finite height over a perfectly conducting plane, where low frequency approximations were incorporated to provide some insight. No numerical results were presented.

We note that in all of the above mentioned papers there existed multiple conductors and/or ground planes, thus assuring the existence of TEM modes. This facilitated developing approximate low frequency approximations if desired. In this paper we deal with the case of a single, infinitely-long wire close to a perpendicular infinite line-current source. As we shall show, the absence of a second conductor or ground plane makes results quite different since no bound modes exist. The analysis presented here is primarily for the infinite current source, with the cases of single and multiple dipole sources presented for comparison purposes.

In the next section we present the analytical formulation of the incident and scattered fields and currents excited on the wire (scatterer). Following that we discuss features of the different complex planes involved in the problem. Next we present asymptotic analysis for obtain-

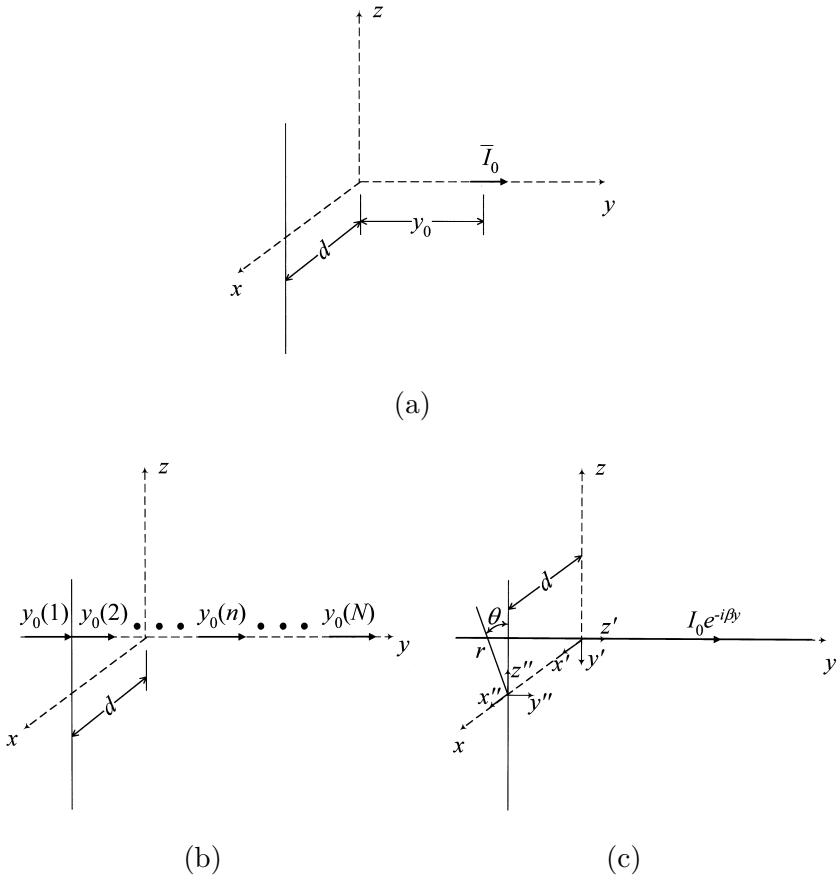

Figure 1. Problem geometry when the source is (a) a dipole, (b) a dipole array, or (c) a line current.

ing approximate expressions for the far-zone field. We also investigate the details of special cases that arise from certain values of parameters. Following that, we specialize the analysis to single and multiple dipole sources and show that we arrive at the continuous source expressions by superimposing the expressions of infinitely many dipoles. Finally, we present the numerical results of the analysis of fields and currents; we show that there is a distinct difference between the radiation patterns of the source and the scatterer. Indeed, the fields generated by the source are heavily attenuated, whereas the fields scattered by the wire do not suffer from such attenuation.

2. FORMULATION

The geometries of the different parts of the problem are shown in Fig. 1. We shall detail the formulation of the continuous source case (Fig. 1c). The current source is assumed to have a constant phase behavior, i.e.,

$$I(y) = I_0 e^{-i\beta y}.$$

where β is a constant. This current form was used many times by Wait (see [11] for example) because it can be extended to a general form current using Fourier transform methods. The single dipole formulation is very similar and that of a dipole array can be obtained by superposition. In the continuous source case we assume that the traveling current speed is slower than that of light in the surrounding medium, i.e., $\beta > k$. In this paper we assume the surrounding medium is free space, although the generalization to any lossless medium can be achieved by incorporating the proper permittivity, so long as β is kept larger than k. The scattering wire is placed a distance d from the source, has a cross-sectional radius a, and is infinitely long. The radius a is assumed sufficiently small to satisfy thin-wire approximations. We split the fields into an incident field emanating from the source, and a scattered field caused by the adjacent wire, viz:

$$\mathbf{E}^{TOTAL} = \mathbf{E}^t = \mathbf{E}^i + \mathbf{E}^s \tag{1}$$

We begin by solving for the incident field. We define (Fig. 1c) a local coordinate system (x', y', z') such that the line current is aligned with the z'-axis, i.e., $x \to x'$, $y \to z', z \to -y'$. Only the z' directed potential is needed. Indeed, if $\mathbf{A}^i$ is the vector potential of the incident field, then

$$\mathbf{A}^i = \mathbf{1}_{z'} \psi^i \tag{2}$$

where

$$\left(\nabla^2_{\rho',z'} + k^2\right) \psi^i = -I_0 e^{-i\beta z'} \frac{\delta(\rho')}{2\pi\rho'}, \tag{3}$$

and $\mathbf{1}_{z'}$ is a unit vector in z' direction. We now define the following Fourier transform pair

$$\begin{aligned} \Psi(\lambda) &= \int_{-\infty}^{\infty} \psi(z') e^{-i\lambda z'} dz' \\ \psi(z') &= \frac{1}{2\pi} \int_{-\infty}^{\infty} \Psi(\lambda) e^{i\lambda z'} d\lambda \end{aligned} \tag{4}$$

and apply the forward transform to (3), viz:

$$\frac{1}{\rho'}\frac{\partial}{\partial\rho'}\left(\rho'\frac{\partial\Psi^i}{\partial\rho'}\right)+\left(k^2-\lambda^2\right)\Psi^i=-I_0\delta(\lambda+\beta)\frac{\delta(\rho')}{\rho'} \tag{5}$$

The solution to (5) is given by [12, eq. 4.116]

$$\Psi^i=\frac{2\pi I_0\delta(\lambda+\beta)}{4i}H_0^{(2)}\left[\left(k^2-\lambda^2\right)^{1/2}\rho'\right] \tag{6}$$

We now take the inverse Fourier transform of (6) to obtain the solution in z', viz:

$$\psi^i=\frac{I_0}{4i}e^{-i\beta z'}H_0^{(2)}(\lambda_0\rho') \tag{7}$$

where

$$\lambda_0=\sqrt{k^2-\beta^2},\ \mathrm{Im}(\lambda_0)<0. \tag{8}$$

In the primed coordinate system, the scatterer is parallel to y', which means that the only electric field component to interact with the wire is $E^i_{y'}$; thus we require only that component, viz:

$$\begin{aligned}E^i_{y'}&=\mathbf{1}_{y'}\cdot\mathbf{E}^i=\left(\mathbf{1}_{\rho'}\sin\phi'+\mathbf{1}_{\phi'}\cos\phi'\right)\cdot\left(\mathbf{1}_{\rho'}E^i_{\rho'}+\mathbf{1}_{\phi'}E^i_{\phi'}+\mathbf{1}_{z'}E^i_{z'}\right)\\&=\sin\phi' E^i_{\rho'}+\cos\phi' E^i_{\phi'}\end{aligned}$$

The required cylindrical components of the field are given by [13, eq. 5–18]

$$\begin{aligned}E^i_{\rho'}&=\frac{1}{\widehat{y}}\frac{\partial^2\psi^i}{\partial\rho'\partial z'},\ \text{and}\\E^i_{\phi'}&=\frac{1}{\widehat{y}\rho'}\frac{\partial^2\psi^i}{\partial\phi'\partial z'}=0\end{aligned}$$

where $\widehat{y}=i\omega\varepsilon$. Thus,

$$\begin{aligned}E^i_{y'}&=\sin\phi'\frac{\partial^2\psi^i}{\partial\rho'\partial z'}\\&=\frac{I_0\beta\lambda_0}{4\widehat{y}}\sin\phi' e^{-i\beta z'}H_1^{(2)}(\lambda_0\rho')\end{aligned} \tag{9}$$

We consider now the scattered field, where we define (Fig. 1c) another local coordinate system (x'',y'',z'') that is just a translated version

of (x, y, z), i.e., $x'' = x - d$. We follow the same steps as with the incident field, but this time the current is unknown. Again

$$\Psi^s = \frac{\mathrm{I}(\lambda)}{4i} H_0^{(2)}(\gamma\rho'')$$

where $\mathrm{I}(\lambda)$ is the Fourier transform of the unknown current, $\gamma = \left(k^2 - \lambda^2\right)^{1/2}$, and $\mathrm{Im}(\gamma) < 0$. We require the scattered field component parallel to the wire, i.e.,

$$E^s_{z''} = \frac{1}{\widehat{y}} \left(\frac{\partial^2}{\partial z''^2} + k^2 \right) \psi^s.$$

In the spectral domain this is given by

$$\begin{aligned} \mathrm{E}^s_{z''} &= \frac{1}{\widehat{y}} \gamma^2 \Psi^s \\ &= \frac{\gamma^2 \mathrm{I}(\lambda)}{4i\widehat{y}} H_0^{(2)}(\gamma\rho''). \end{aligned} \tag{10}$$

We now apply the inverse Fourier transform to (10) to obtain

$$E^s_{z''} = \frac{1}{8\pi i\widehat{y}} \int_{-\infty}^{\infty} \gamma^2 \mathrm{I}(\lambda) H_0^{(2)}(\gamma\rho'') e^{i\lambda z''} d\lambda \tag{11}$$

In order to evaluate $\mathrm{I}(\lambda)$ we apply the boundary condition on the surface of the scatterer, i.e.,

$$E^t \mid_{\text{tangential}} = \left[E^i + E^s\right]_{\text{tangential}} = 0 \tag{12}$$

To do this we transform the coordinates (x'', y'', z'') to (x', y', z'), i.e., $x'' \to x' - d$, $y'' \to z'$, and $z'' \to -y'$. Thus,

$$\rho'' = \left(x''^2 + y''^2\right)^{1/2} \to \left[\left(x' - d\right)^2 + z'^2\right]^{1/2}$$

and with changing λ to $-\lambda$, (11) becomes

$$E^s_{y'} = \frac{1}{8\pi i\widehat{y}} \int_{-\infty}^{\infty} \gamma^2 \mathrm{I}(-\lambda) H_0^{(2)} \left\{ \gamma \left[\left(x' - d\right)^2 + z'^2\right]^{1/2} \right\} e^{i\lambda y'} d\lambda \tag{13}$$

For the application of the boundary condition, we evaluate (9) at the center of the wire $(x' = d,\ z' = 0)$, and (13) at the surface of the wire $\left(\left[(x'-d)^2 + z'^2\right]^{1/2} = a\right)$. This is valid so long as $a \ll \lambda_m$, and $d \gg a$, where $\lambda_m = 2\pi/k$. Then from (12), (9), and (13) we get

$$\begin{aligned}
&\frac{1}{2\pi i}\int_{-\infty}^{\infty} \gamma^2 \mathrm{I}(-\lambda) H_0^{(2)}(\gamma a) e^{i\lambda y'} d\lambda \\
&\quad = -I_0 \beta \lambda_0 \frac{y'}{\left(d^2 + y'^2\right)^{1/2}} H_1^{(2)}\left[\lambda_0 \left(d^2 + y'^2\right)^{1/2}\right] \\
&\quad = I_0 \beta \frac{\partial}{\partial y'} H_0^{(2)}\left[\lambda_0 \left(d^2 + y'^2\right)^{1/2}\right] \qquad (14)
\end{aligned}$$

We now apply the forward transform defined in (4) on both sides of (14) with respect to y', viz:

$$\gamma^2 \mathrm{I}(-\lambda) H_0^{(2)}(\gamma a) = -I_0 \beta \lambda \mathcal{F}\left\{H_0^{(2)}\left[\lambda_0 \left(d^2 + y'^2\right)^{1/2}\right]\right\} \qquad (15)$$

where $\mathcal{F}\{\cdot\}$ denotes the Fourier transform operator. The transform of $H_0^{(2)}$ is obtained through a well-known integral identity [12, eq. 4.306]; thus (15) becomes

$$\gamma^2 \mathrm{I}(-\lambda) H_0^{(2)}(\gamma a) = -2 I_0 \beta \lambda \frac{e^{-id\left(\lambda_0^2 - \lambda^2\right)^{1/2}}}{\left(\lambda_0^2 - \lambda^2\right)^{1/2}}$$

Rearranging yields

$$\mathrm{I}(\lambda) = \frac{2 I_0 \beta \lambda e^{-id\widehat{\gamma}}}{\gamma^2 \widehat{\gamma} H_0^{(2)}(\gamma a)} \qquad (16)$$

where

$$\widehat{\gamma} = \left(\lambda_0^2 - \lambda^2\right)^{1/2} \qquad (17)$$

and $\mathrm{Im}\left(\widehat{\gamma}\right) < 0$. From (16) and (13) we obtain the complete expression for $E_{y'}^s$, viz:

$$E_{y'}^s = -\frac{I_0 \beta}{4\pi i \widehat{y}} \int_{-\infty}^{\infty} \frac{\lambda H_0^{(2)}\left\{\gamma\left[(x'-d)^2 + z'^2\right]^{1/2}\right\}}{H_0^{(2)}(\gamma a)} \frac{e^{-id\widehat{\gamma}}}{\widehat{\gamma}} e^{i\lambda y'} d\lambda \qquad (18)$$

Now that we have both the incident and scattered fields in the primed system, we transform back to the original unprimed system to cast the equations in their desired forms $(x' \to x,\ y' \to -z,\ z' \to y)$. Note that because $y' \to -z$, we have to multiply the expressions by a minus sign to get the correct sign of the z-component, viz:

$$E_z^i = -\frac{I_0 \beta \lambda_0}{4\widehat{y}} \frac{z}{\left(x^2+z^2\right)^{1/2}} e^{-i\beta y} H_1^{(2)}\left(\lambda_0 \left(x^2+z^2\right)^{1/2}\right) \tag{19}$$

and

$$E_z^s = \frac{I_0 \beta}{4\pi i \widehat{y}} \int_{-\infty}^{\infty} \frac{\lambda H_0^{(2)}\left\{\gamma\left[(x-d)^2+y^2\right]^{1/2}\right\}}{H_0^{(2)}(\gamma a)} \frac{e^{-id\widehat{\gamma}}}{\widehat{\gamma}} e^{-i\lambda z} d\lambda. \tag{20}$$

In order to get the familiar form of the inverse Fourier transform we change λ to $-\lambda$, viz:

$$E_z^s = -\frac{I_0 \beta}{4\pi i \widehat{y}} \int_{-\infty}^{\infty} \frac{\lambda H_0^{(2)}\left\{\gamma\left[(x-d)^2+y^2\right]^{1/2}\right\}}{H_0^{(2)}(\gamma a)} \frac{e^{-id\widehat{\gamma}}}{\widehat{\gamma}} e^{i\lambda z} d\lambda. \tag{21}$$

To obtain the excited current as a function of z, we note that (16) was obtained by operating on y'. Thus we have to apply the same procedure followed in obtaining the fields regarding coordinate transformations, viz:

$$I(z) = -\frac{I_0 \beta}{\pi} \int_{-\infty}^{\infty} \frac{\lambda e^{-id\widehat{\gamma}}}{\gamma^2 \widehat{\gamma} H_0^{(2)}(\gamma a)} e^{i\lambda z} d\lambda \tag{22}$$

3. FEATURES OF COMPLEX PLANES

Here we explain the details of the complex planes involved in solving the continuous source case; then we specialize to the dipole case. The complex plane of (21) and (22) is shown in Figure 2. We shall defer discussion of the contours $\mathrm{C_I}$ and $\mathrm{C_{II}}$ until the numerical results section. There are three branch cuts in this plane: The first is $\mathrm{Im}\,(\gamma) = 0$ where $\gamma = \left(k^2-\lambda^2\right)^{1/2}$. The branch points are $\lambda = \pm k$ and the branch cut covers the whole imaginary axis and the piece of real axis

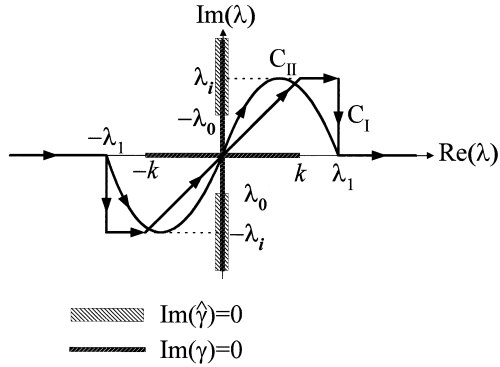

Figure 2. Complex λ-plane showing branch cuts and numerical integration contours.

between branch points. The second branch cut is $\mathrm{Im}\,(\widehat{\gamma}) = 0$ where $\widehat{\gamma} = \left(k^2 - \beta^2 - \lambda^2\right)^{1/2}$. The branch points are $\lambda = \pm\lambda_0$ (see (8)) and the branch cut $\in (-i\infty, \lambda_0] \cup [-\lambda_0, i\infty)$. Finally, the third branch cut is the one associated with the Hankel functions in (21) and (22), defined by $\mathrm{Im}\,(\gamma) = 0$ and $\mathrm{Re}\,(\gamma) < 0$. This branch cut lies on top of the first one but is of a different nature. The first branch cut is a square root represented by a two-sheet Riemann surface, while the third has a logarithmic nature near the origin represented by an infinitely sheeted Riemann surface. To insure convergence of (21) and (22), we define the top sheet of the complex λ-plane as $\mathrm{Im}\,(\gamma) < 0$ and $\mathrm{Im}\,(\widehat{\gamma}) < 0$. Furthermore, to achieve proper phase we require that the contour of integration pass through the third and first quadrants of the λ-plane where $\mathrm{Re}\,(\gamma) > 0$ and $\mathrm{Re}\,(\widehat{\gamma}) > 0$. More details about λ and γ complex planes can be found in Chapter 3 of [14].

In the continuous source case, steepest descent analysis is performed first by applying the usual mapping to the scattering integral (21):

$$\lambda = k \sin w. \tag{23}$$

We then take $kr \gg 1$, where r is the distance from $(d, 0, 0)$ to the observer. The complex w-plane is shown in Figure 3, where we note that γ becomes an analytic function. However, the branch cut associated with the Hankel functions does not disappear. Note that since the branch point of $\widehat{\gamma}$ depends on β, the branch point becomes very close to the origin for values of $\beta/k \approx 1$. In this situation the steepest

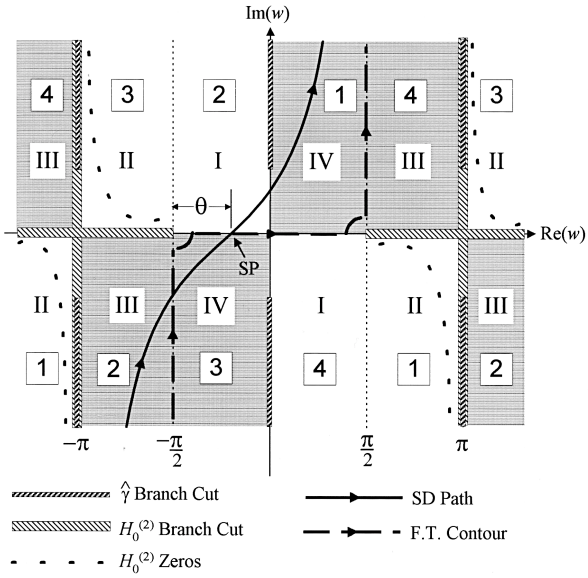

Figure 3. Steepest descent complex plane.

descent path intersects the branch cut for most values of θ. In general, the SD path does intersect the branch cut near grazing ($\theta \to 0$) for all values of β. In the dipole case, the w plane has no $\widehat{\gamma}$ branch cut, which means that there is no difficulty with the SD path intersecting it. All other features in the w and λ planes are the same as the continuous source case. One final note here is that the SD path shown in Figure 3 corresponds to $kr \gg 1$ and $r/d \gg 1$. For $r/d > 1$ but not very large, the situation is different. The details are in the next section.

4. ASYMPTOTIC ANALYSIS

In this section we shall first consider the asymptotic analysis of (21). We shall assume that both kr and r/d are much greater than 1. Later on we shall relax the second condition. We use the method of steepest descents as described in [15] by applying (23) and the usual coordinate transformation $z = r\cos\theta$ and $\left[(x-d)^2 + y^2\right]^{1/2} = r\sin\theta$ to (21), viz:

$$E_z^s = -\frac{I_0\beta k^2}{4\pi i\widehat{y}}\int_{FTC}\frac{\sin w\cos w H_0^{(2)}\left(kr\cos w\sin\theta\right)}{H_0^{(2)}(ka\cos w)}\ \frac{e^{-id\widehat{\gamma}}}{\widehat{\gamma}}e^{ikr\sin w\cos\theta}dw, \tag{24}$$

where r and θ are as indicated in Figure 1c, $\widehat{\gamma} = \left[(k\cos w)^2 - \beta^2\right]^{1/2}$, and FTC denotes the Fourier transform contour shown in Figure 3. We take $kr \gg 1$ and invoke the large argument approximation for the Hankel function [16, eq. 9.2.4] in the numerator, viz:

$$E_z^s \approx \int_{FTC} f(w)e^{g(w)}dw, \tag{25}$$

where

$$g(w) = ikr\sin(w-\theta),\ \text{and} \tag{26}$$

$$f(w) = -e^{i\pi/4}\frac{I_0\beta k^2\sin w\cos w e^{-id\widehat{\gamma}}}{4\pi i\widehat{y}\widehat{\gamma}H_0^{(2)}(ka\cos w)\left(\dfrac{\pi kr\sin\theta\cos w}{2}\right)^{1/2}}. \tag{27}$$

The next step is to deform FTC to the SD path defined along the valleys of

$$\cosh\left(\operatorname{Im} w\right) = -\csc\left(\operatorname{Re} w - \theta\right). \tag{28}$$

In doing this, we do not encounter any singularities for most values of θ and β. For values of $\theta \to 0$ the SD path may have to wrap around the $\widehat{\gamma}$ branch cut located on the positive imaginary w-axis. We shall consider this subsequently. The saddle point (SP) lies at $w_0 = m\pi/2 + \theta$, m odd, where we pick $m = -1$ to make the range of w around the origin. By standard SD techniques we evaluate $f(w)$ at SP and perform the integral along the SD path to yield

$$E_{z,SP}^s = -I_0\eta_m\frac{e^{-ikr}}{2\pi r}\frac{\beta}{k}\frac{\cos\theta}{H_0^{(2)}\left(ka\sin\theta\right)}\frac{e^{-kd\left[\left(\frac{\beta}{k}\right)^2-\sin^2\theta\right]^{1/2}}}{\left[\left(\dfrac{\beta}{k}\right)^2-\sin^2\theta\right]^{1/2}} \tag{29}$$

where η_m is the intrinsic impedance of the medium (free space here). The SP contribution gives an excellent approximation of the scattered

field for $kr > 20\pi, r/d > 10, \beta/k \geq 1.11,$ and $0.1 < \theta/\pi \leq 0.5$. This combination of values guarantees that the observer is well in the *far zone* and away from grazing angles. Mathematically this means that the SD path does not wrap around the $\widehat{\gamma}$ branch cut and is not near the Hankel function branch cut. Strictly speaking, in this problem there is no *far zone region*, because the scatterer has infinite length. However, if the observer is not close to grazing, the SP approximation can be made very close to the actual field if kr is large enough. It is instructive to modify the standard SP approximation for parameters other than ones mentioned above.

A. $1 < \beta/k < 1.11$

In this case, the $\widehat{\gamma}$ branch point becomes very close to the origin of the w-plane. For example, if $\beta/k = 1.01$, the branch point is at $w = i\cosh^{-1}(\beta/k) \approx i0.14$. This means that for most values of θ the SD path will wrap around a portion of the $\widehat{\gamma}$ branch cut, producing a contribution that must be added to the SP approximation. Initially the SD path meets the branch cut at $iw_1 = i\cosh^{-1}(\csc\theta)$; then to stay on the proper sheet, it goes down the branch cut, wraps around the branch point $iw_2 = i\cosh^{-1}(\beta/k)$, goes up along the other side of the branch cut to iw_1, then continues on the SD path. Along the path around branch cut, $\mathrm{Im}(\widehat{\gamma}) = 0$ and $\mathrm{Re}(\widehat{\gamma})$ is negative on the downward portion and positive on the upward. From the above information, we use (25) to formulate the branch cut integral, viz:

$$E^s_{z,BC} = C_{BC}\int_{w_2}^{w_1} \frac{\sinh w_i\,(\cosh w_i)^{1/2}\cos(d\widehat{\gamma})e^{ikr\sin(iw_i-\theta)}}{\widehat{\gamma}H_0^{(2)}(ka\cosh w_i)}dw_i \quad (30)$$

where

$$C_{BC} = \frac{e^{i\pi/4}I_0\beta k^2}{i\pi\widehat{y}\,(2\pi kr\sin\theta)^{1/2}}\ ,$$

and $\widehat{\gamma} = \left[k^2\cosh^2 w_i - \beta^2\right]^{1/2}$, a real positive quantity along integration path. Since the branch point w_2 is our main concern here, we follow Ishimaru's method [17, Section 15–8] in expanding relevant terms in the integrand around it, while evaluating other terms without

expansion[1]. In particular, the following expansions are performed

$$\begin{aligned}
\cos(d\widehat{\gamma}) &\approx 1 - \frac{\beta}{k}(kd)^2 \chi (w_i - w_2) \qquad (31)\\
\widehat{\gamma} &\approx k\left[2\frac{\beta}{k}\chi (w_i - w_2)\right]^{1/2}\\
\sin(iw_i - \theta) &\approx -\alpha_1 + i\alpha_2 (w_i - w_2), \text{ where}\\
\alpha_1 &= \frac{\beta}{k}\sin\theta - i\chi\cos\theta,\\
\alpha_2 &= \frac{\beta}{k}\cos\theta + i\chi\sin\theta, \text{ and}\\
\chi &= \left[\left(\frac{\beta}{k}\right)^2 - 1\right]^{1/2}.
\end{aligned}$$

We shall call the result *Ishimaru's approximation* (IA), viz:

$$E_{IA} = C_{IA}\int_{w_2}^{w_1}\left[1 - \frac{\beta}{k}(kd)^2\chi(w_i - w_2)\right]\frac{e^{-kr\alpha_2(w_i - w_2)}}{(w_i - w_2)^{1/2}}dw_i \qquad (32)$$

where

$$C_{IA} = C_{BC}\frac{e^{-ikr\alpha_1}}{kH_0^{(2)}(\beta a)}\left(\frac{\chi}{2}\right)^{1/2}.$$

If w_1 is finite (the SD path wraps around a portion of the branch cut), then (32) can be expressed in terms of incomplete gamma functions, which we develop into a series for computational purposes. However, as $\theta \to 0, w_1 \to \infty$, and the SD path wraps around the whole branch cut. In this case we can express (32) in terms of $\Gamma(1/2)$ and $\Gamma(3/2)$ [16, eq. 6.1.1], viz:

$$E_{IA} = H(\epsilon)C_{IA} \times \begin{cases} 2e^{-\alpha\epsilon}\epsilon^{1/2}(1 + S\Omega), & \text{if } \theta > \theta_0 \text{ (or } w_2 < w_1 < \infty) \\ \left(\frac{\pi}{\alpha}\right)^{1/2}\Omega, & \text{if } \theta < \theta_0 \text{ (or } w_1 \to \infty) \end{cases} \qquad (33)$$

[1] The approach we follow here is slightly different from that of Ishimaru. Our approach does not produce caustic behavior as $w_2 \to w_1$ because of the way we handle the branch cut integral.

where

$$\alpha = kr\alpha_2,$$
$$\Omega = 1 - \frac{\beta}{2\alpha k}(kd)^2 \chi,$$
$$S = \sum_{m=1}^{\infty} \frac{m!}{(2m+1)!}(4\alpha\epsilon)^m,$$
$$\epsilon = w_1 - w_2,$$
$$\frac{\pi}{2} > \theta_0 > \sin^{-1}\left[\operatorname{sech}\left(\frac{2}{\delta} + w_2\right)\right],$$
$$\delta = 2\alpha(\Omega - 1),$$

and $H(\cdot)$ is the Heaviside unit step function, which is inserted to draw the readers attention to the fact that the branch cut contribution is computed only when $\csc(\theta) > \beta/k$. The lower limit on θ_0 is determined by limiting the second term of the cosine expansion in (31) to 2. For most combinations of parameters, this limit is too stringent (almost 0). A more computationally convenient value is $0.1\,\pi$. Note that $E_{IA} \to 0$ as $w_2 \to w_1$ because when SD path wraps around a finite length of branch cut, we properly handle the integral as a finite integral. In [17], Ishimaru extends the path to infinity, then crosses the branch cut to the proper sheet in order to complete the SD path. This introduces false caustic behavior when $w_2 \to w_1$.

As we shall show in numerical results, this approximation is only valid for small values of d/r (< 0.2), because of the series in d^2 that results from (31). To expand the envelope of approximation, we must then add more terms of this series, complicating the resulting integral. We may obtain a better approximation of (30) by not expanding the cosine function. We begin by splitting (30) into two integrals, viz:

$$E_{BC} = \frac{C_{BC}}{2}\left(E^+ + E^-\right) \tag{34}$$

where

$$E^{\pm} = \int_{w_2}^{w_1} \frac{\sinh w_i \left(\cosh w_i\right)^{1/2} e^{\pm id\widehat{\gamma}} e^{ikr\sin(iw_i - \theta)}}{\widehat{\gamma} H_0^{(2)}(ka\cosh w_i)} dw_i. \tag{35}$$

Now we only expand the sine function and $\widehat{\gamma}$ and evaluate everything else at w_2, viz:

$$E^{\pm} \approx \overline{C} \int_{w_2}^{w_1} \frac{e^{\pm\overline{\alpha}(w_i - w_2)^{1/2}} e^{-\alpha(w_i - w_2)}}{(w_i - w_2)^{1/2}} dw_i \tag{36}$$

where

$$\overline{C} = \frac{e^{-ikr\alpha_1}}{kH_0^{(2)}(\beta a)} \left(\frac{\chi}{2}\right)^{1/2}, \text{ and}$$

$$\overline{\alpha} = ikd \left(2\chi \frac{\beta}{k}\right)^{1/2}.$$

The integral in (36) can be expressed in terms of error functions [16, eq. 7.1.1], viz:

$$E^{\pm} \approx \overline{C} \left(\frac{\pi}{\alpha}\right)^{1/2} e^{\overline{\alpha}^2/4\alpha} \left[\text{erf}\left(\frac{\mp\overline{\alpha}}{2\alpha^{1/2}} + (\alpha\epsilon)^{1/2}\right) - \text{erf}\left(\frac{\mp\overline{\alpha}}{2\alpha^{1/2}}\right)\right] \quad (37)$$

Substituting (37) in (34) yields the required improved branch cut contribution, viz:

$$E_{BC,imp} = C_{imp} \left[\text{erf}\left((\alpha\epsilon)^{1/2} - \frac{\overline{\alpha}}{2\alpha^{1/2}}\right) + \text{erf}\left((\alpha\epsilon)^{1/2} + \frac{\overline{\alpha}}{2\alpha^{1/2}}\right)\right] \quad (38)$$

where

$$C_{imp} = H(\epsilon) \frac{-e^{i\pi/4} I_0 \beta\eta}{4\pi k H_0^{(2)}(\beta a)} \left(\frac{\chi}{\alpha_2 \sin\theta}\right)^{1/2} \frac{e^{-ik\alpha_1 r}}{r}, \text{ and} \quad (39)$$

$$\text{erf}(z) = \frac{2}{\pi^{1/2}} \int_0^z e^{-t^2} dt. \quad (40)$$

This approximation has the proper behavior when $kd \gg 1$; since as $\overline{\alpha} \to \infty$, $E_{BC,imp} \to 0$.

We next investigate what the branch cut contribution physically produces in the scattered electric field. When $kd \to 0$, $\overline{\alpha} \to 0$, and we gain more insight by examining the branch point contribution in cylindrical coordinates. Letting $\rho = r\sin\theta$ and $z = r\cos\theta$ in (38) and applying the definitions of α, α_1, and α_2, we produce

$$E_{BC,imp} \to \overline{C}_{imp} \frac{e^{-i\beta\rho}}{\rho^{1/2}} \frac{e^{-kz\chi}}{\left(\frac{\beta}{k}z + i\rho\chi\right)^{1/2}} \text{erf}\left[\left\{\epsilon k \left(\frac{\beta}{k}z + i\rho\chi\right)\right\}^{1/2}\right] \quad (41)$$

where

$$\overline{C}_{imp} = H(\epsilon) \frac{-e^{i\pi/4} I_0 \beta\eta}{4\pi k} \frac{\chi^{1/2}}{H_0^{(2)}(\beta a)}$$

Thus in the low frequency limit, the branch cut contribution manifests itself as a cylindrical wave modified by phase and amplitude factors. The role of the error function can be made clearer for some limiting cases. For grazing angles, $\theta \to 0$ and $\epsilon \to \infty$; thus $\mathrm{erf}(\cdot) \to 1$. Here the wave propagates in ρ with a speed slower than that of light in the surrounding medium, and attenuates in $|z|$. Although the derivation here was made for positive z, the behavior in negative z is the same because of symmetry. The spatial spread is not exactly that of a pure cylindrical wave. When the observer is close to broadside ($\theta \to \pi/2$) the argument of the error function is very small (because the steepest descents path wraps around a very small portion of the branch cut). Thus $\mathrm{erf}(z) \to \left(2z/\pi^{1/2}\right)\exp(-z^2)$, and

$$E_{BC} \to 2\overline{C}_{imp}\left(\frac{k\epsilon}{\pi}\right)^{1/2}\frac{e^{-i\rho(\beta+k\epsilon x)}}{\rho^{1/2}}e^{-z(k\chi+\epsilon\beta)} \tag{42}$$

which is a cylindrical wave localized to the plane normal to the scatterer.

The above two approximations take care of the branch cut contribution when the SD path wraps around it, but they do nothing to the SP contribution itself when the SP approaches the branch point. The SD approximation assumes that the SP has the most contribution to the scattering integral; but when the SP is close to λ_0, this is no longer valid, especially if d/r is not very small. Both the SP location and the SD path slope change as a result of proximity of the branch point. One way to include the effect of a branch point proximity to a SP is to apply a method first suggested by Bleistein [18] and explained later for this special case by Felsen and Marcuvitz [15, Section 4.4c]. This method accommodates the effect of *algebraic* branch points near saddle points and assumes no change in SP location or SD slope. Although in our case the branch point is more than algebraic ($\widehat{\gamma}$ is also in an exponent), we shall still use the method for illustrative purposes. We begin from (25) and evaluate everything but the second exponent and algebraic branch cut at w_0, viz:

$$E_z^s \approx h(w_0)\int_{SD}\frac{e^{ikr\sin(w-\theta)}}{\left[\cos^2 w-\left(\frac{\beta}{k}\right)^2\right]^{1/2}}dw, \tag{43}$$

where

$$h(w_0) = e^{i\pi/4} \frac{I_0 \beta k \cos\theta e^{-id\left[(k\sin\theta)^2 - \beta^2\right]^{1/2}}}{4\pi i \widehat{y} H_0^{(2)}(ka\sin\theta) \left(\frac{\pi kr}{2}\right)^{1/2}}.$$

Since the above integral is significant only around w_0, we employ the change of variables $u = w - \theta + \pi/2$ and expand around $u = 0$, viz:

$$E_z^s \approx h(w_0) \int_{\nearrow} \frac{e^{-ikr(1-u^2/2)}}{\left[\sin^2\theta + u\sin 2\theta - \left(\frac{\beta}{k}\right)^2\right]^{1/2}} du \tag{44}$$

where the slanted arrow denotes the 45° local slope of the SD path at $u = 0$. In the vicinity of $u = 0$, the real part of the square root in the denominator of (44) changes sign from lower limit of integration to upper limit. This necessitates splitting the integral into two parts; we also use same reasoning of asymptotic analysis to extend each part to infinity. The above integral can be then expressed in terms of parabolic cylinder functions as follows

$$E_{MSP} = C_{MSP}\left[D_{-\frac{1}{2}}\left(b\,(kr)^{1/2}\right) + iD_{-\frac{1}{2}}\left(-b\,(kr)^{1/2}\right)\right] \tag{45}$$

where

$$b = \frac{\left(\frac{\beta}{k}\right)^2 - \sin^2\theta}{\sin 2\theta} e^{i3\pi/4}, \tag{46}$$

$$C_{MSP} = \frac{I_0 \beta \eta e^{-i\pi/8}}{4\pi\,(kr)^{3/4}} (\cot\theta)^{1/2} \frac{e^{-kd\left[\left(\frac{\beta}{k}\right)^2 - \sin^2\theta\right]^{1/2}}}{H_0^{(2)}\,(ka\sin\theta)} e^{-ikr(1-|b|^2/4)},$$

and the parabolic cylinder function is given by [15, eq. 4.5.36]

$$D_{-\nu}(t) = \frac{2e^{t^2/4}}{\Gamma\,(\nu)} \int_0^\infty p^{2\nu-1} e^{-\frac{1}{2}(p^2+t)^2} dp, \qquad Re\,(\nu) > 0.$$

The steps needed to arrive from (44) to (45) are elaborate and can be found in Appendix A of [14].

Although there is some improvement introduced by (45) over the standard SP approximation, the field still deviates from numerically

computed fields at certain angles and for some combinations of parameters. This is due to the assumption that neither the SP location nor the SD path change when approaching the $\widehat{\gamma}$ branch point. If we employ the large argument expansion of $D_{-\nu}(t)$ [19, Section 16.52], then we get back the standard SP contribution previously derived in (29).

B. $\theta \to \pi/2$

Here we show why both standard and modified SD analyses fail to give the correct field for angles approaching scatterer broadside. The deviation is observed for $\beta/k \approx 1$ and $r/d < 10$. To show this, we go back to (25) where we include both exponents into our attempt to find a correct SD analysis, i.e.,

$$g(w) = ikr\sin(w-\theta) - ikd\left[\cos^2 w - \left(\frac{\beta}{k}\right)^2\right]^{1/2}. \tag{47}$$

To find SP we set $\partial g/\partial w = 0$, viz:

$$\cos(w_0-\theta) = -\frac{d}{r}\frac{\cos w_0 \sin w_0}{\left[\cos^2 w_0 - \left(\frac{\beta}{k}\right)^2\right]^{1/2}}. \tag{48}$$

Note that for $d/r \to 0$ we get back the result obtained before. However, if this is not the case and d is comparable to r then (48) is a transcendental equation that is not easily treated analytically. We may obtain a feeling for the situation by assuming a value for θ and examining w_0. If $\theta = \pi/2$, then (48) can be simplified as

$$\left[\cos^2 w_0\left\{1-\left(\frac{d}{r}\right)^2\right\} - \left(\frac{\beta}{k}\right)^2\right]\sin^2 w_0 = 0$$

which has the solution

$$w_0 = m\pi \text{ and } m\pi \pm i\cosh^{-1}\left[s\frac{\beta}{k}\left(\frac{1}{1-(d/r)^2}\right)^{1/2}\right],\ m = 0, \pm1, \pm2, ...$$

where $s = \pm(-1)^m$. The upper (lower) sign in s is chosen when m is even (odd). This shows that for every value of m there are *three*

saddle points instead of one. For example, if $m = 0$ we have the original SP at $w_0 = 0$ and two other SP's on the imaginary axis on either side of the origin. For other values of θ, a complex plane root search must be employed to find the two SP's off real axis. If these are found, one can use the approach in [15, Section 4.5b] to find the effect of three neighboring SP's. We leave this for future work.

C. $\theta < 0.1\pi$

When θ becomes smaller and approaches grazing, another behavior appears in the numerically integrated scattered field that does not appear in standard or modified SD approximation. This behavior exists in all combinations of $\beta, d,$ and r but is sometimes masked by a stronger SP contribution. The behavior is manifested by oscillations on top of the scattered field envelope; the oscillations increase in magnitude as $\theta \to 0$. We show representative plots of this in the numerical results section. We may examine what is happening by looking at Figure 3. As $\theta \to 0$, the SD path moves towards the left and the SP approaches $w = -\pi/2,$ which is the location of the Hankel function branch point. Also, the upper part of the SD path is now wrapped around more of the $\widehat{\gamma}$ branch cut. The oscillations we observe are not accommodated by the branch cut contribution; so it must be the effect of the Hankel function branch point. We expect that because the branch point is logarithmically singular, it has a nontrivial effect on both the SP location and the constant phase path. For some combinations of parameters, the SP contribution is orders of magnitudes lower than the oscillations. The analysis of the situation is further complicated if we take into account the other two SP's we discussed above. Physically, these oscillations appear because the observer is closer to the scattering wire but far from its center. We shall show later that along the wire there is always an excitation of traveling currents that will cause these oscillations when the observer is close to the wire.

5. DIPOLE SOURCE EXCITATION

Here we simply mention the final formulas obtained if the excitation is a dipole source. The derivation is similar but simpler than that of the continuous source case. If a dipole source is placed as shown in Figure 1a, then the incident field is given by [13, eq. 2-113]

$$E^i_{Dz} = \frac{\overline{I}_0 l}{2\pi} e^{-ik\left[x^2+(y-y_0)^2+z^2\right]^{1/2}} \frac{(y-y_0)\,z}{x^2+(y-y_0)^2+z^2} \times \left[\frac{3}{2}\left(\frac{\eta}{x^2+(y-y_0)^2+z^2} + \frac{1}{i\omega\epsilon\left[x^2+(y-y_0)^2+z^2\right]^{3/2}}\right) + \frac{i\omega\mu}{2\left[x^2+(y-y_0)^2+z^2\right]^{1/2}}\right]$$

where the subscript D designates dipole quantities, l is dipole length, and $\overline{I}_0 = I_0(\omega)f(y_0)$ is an arbitrary function of the operating frequency ω and dipole position y_0. An alternative form used to match boundary conditions can be obtained from an equivalent form [3]:

$$E^i_{Dz} = -\frac{\overline{I}_0 l}{8\pi\widehat{y}} \frac{y-y_0}{\left[x^2+(y-y_0)^2\right]^{1/2}} \int_{-\infty}^{\infty} \lambda\gamma H_1^{(2)}\left[\gamma\left(x^2+(y-y_0)^2\right)\right]^{1/2} e^{i\lambda z} d\lambda \tag{49}$$

By matching boundary conditions on the surface of the wire, we obtain the excited current and scattered field, viz:

$$I_D(z) = \frac{\overline{I}_0 l}{i2\pi} \frac{y_0}{\left(d^2+y_0^2\right)^{1/2}} \int_{-\infty}^{\infty} \lambda \frac{H_1^{(2)}\left[\gamma\left(d^2+y_0^2\right)^{1/2}\right]}{\gamma H_0^{(2)}(\gamma a)} e^{i\lambda z} d\lambda, \text{ and} \tag{50}$$

$$E^s_{Dz} = -\frac{\overline{I}_0 l}{8\pi\widehat{y}} \frac{y_0}{\left(d^2+y_0^2\right)^{1/2}} \int_{-\infty}^{\infty} \lambda\gamma \frac{H_1^{(2)}\left[\gamma\left(d^2+y_0^2\right)^{1/2}\right]}{H_0^{(2)}(\gamma a)} H_0^{(2)}\left(\gamma\left[(x-d)^2+y^2\right]^{1/2}\right) e^{i\lambda z} d\lambda \tag{51}$$

The current and field for the dipole array case are obtained by superimposing the above two equations. We demonstrate this for the current. Suppose that we want the current on the wire excited by an array of N

dipoles placed tip to tail on the y-axis from $-Y_0$ to $+Y_0$, where we restrict N to be even (Figure 1b). Such a configuration will have $N/2$ dipoles on each side of the y-axis with no dipole placed at the origin. If all the dipoles are of equal lengths ($l_1 = l_2 = \cdots = l_N = l$), then the spacing between each dipole and its neighbor is $\Delta y = l = 2Y_0/(N-1)$. Also, the position of each dipole will be given by

$$y_0(n) = -Y_0 \left(\frac{N-2n}{N-2} \right) - \Delta y \left(\frac{n-1}{N-2} \right), \; n = 1, 2, \ldots, N$$

In this development we also make the current strength of each dipole a phased function of the position, i.e., $\overline{I}_0 = I_0 e^{-i\beta y_0(n)}$, where I_0 is a function of the operating frequency. The spatial-frequency current excited by the array thus can be expressed as the following Riemann sum

$$\begin{aligned} \mathrm{I}_A(\lambda) = \frac{I_0 \lambda \Delta y}{i\gamma H_0^{(2)}(\gamma a)} \sum_{n=1}^{N} e^{-i\beta y_0(n)} \frac{y_0(n)}{(d^2 + y_0(n)^2)^{1/2}} \\ \cdot H_1^{(2)} \left(\gamma \left[d^2 + y_0(n)^2 \right]^{1/2} \right) \end{aligned} \tag{52}$$

where A denotes the dipole array. If we take $N \to \infty$, then $\Delta y \to dy$, $y_0(n) \to y$, and the sum becomes an integral from $-Y_0$ to $+Y_0$. If we further take $Y_0 \to \infty$ then we get

$$\mathrm{I}_A(\lambda) = \frac{I_0}{i\gamma H_0^{(2)}(\gamma a)} \lambda \int_{-\infty}^{\infty} e^{-i\beta y} H_1^{(2)} \left(\gamma \left[d^2 + y^2 \right]^{1/2} \right) \frac{y}{(d^2 + y^2)^{1/2}} dy \tag{53}$$

Integrating by parts and using a well known identity of Hankel functions [12, eq. 4.306], the above equation can be expressed as

$$\mathrm{I}_A(\lambda) = -\frac{I_0}{i\gamma^2 H_0^{(2)}(\gamma a)} \lambda i\beta \left(\frac{2ie^{-d(\beta^2 - \gamma^2)^{1/2}}}{(\beta^2 - \gamma^2)^{1/2}} \right) \tag{54}$$

By letting $i\widehat{\gamma} = (\beta^2 - \gamma^2)^{1/2}$ where $\mathrm{Im}(\widehat{\gamma}) < 0$ and taking the inverse Fourier transform we get

$$I_A(z) = -\frac{\beta I_0}{\pi} \int_{-\infty}^{\infty} \frac{\lambda e^{-id\widehat{\gamma}}}{\gamma^2 \widehat{\gamma} H_0^{(2)}(\gamma a)} e^{i\lambda z} d\lambda. \tag{55}$$

This is the same current expression derived in the continuous source problem.

The asymptotic behavior of the scattered field excited by a single dipole is given by

$$E^s_{Dz,SD} = \frac{\overline{I}_0 l k^2}{4\pi\omega\epsilon} \frac{y_0}{\left(d^2+y_0^2\right)^{1/2}} \frac{e^{-ikr}}{r} \cos\theta \sin\theta \frac{H_1^{(2)}\left[k(\sin\theta)\left(d^2+y_0^2\right)^{1/2}\right]}{H_0^{(2)}(ka\sin\theta)}. \tag{56}$$

For dipole excitation, the situation is simpler than the continuous source case because we do not have a branch cut intercepting the SD path and the Hankel function branch point has a much weaker effect. An observation worth mentioning is that the SP contribution begins to have a good agreement with numerical integration for $r/\left(d^2+y_0^2\right)^{1/2} > 100$. The reason is that the current excited on the wire from a single dipole has a non-localized behavior, unlike some cases of the dipole array and continuous source cases where we can achieve localized current behavior. We shall explain this further in the next section.

Finally, the current excited by a single dipole has a logarithmic asymptotic behavior. We show this by casting (50) as

$$I_D(z) = -\frac{\overline{I}_0 l}{2\pi} \frac{y_0}{\left(d^2+y_0^2\right)^{1/2}} \frac{\partial}{\partial z} \int_{-\infty}^{\infty} \frac{H_1^{(2)}\left[\gamma\left(d^2+y_0^2\right)^{1/2}\right]}{\gamma H_0^{(2)}(\gamma a)} e^{i\lambda z} d\lambda \tag{57}$$

The integral in the above equation has been shown [20, 21] to have the following asymptotic behavior as $z \to \infty$

$$\int_{-\infty}^{\infty} \frac{H_1^{(2)}\left[\gamma\left(d^2+y_0^2\right)^{1/2}\right]}{\gamma H_0^{(2)}(\gamma a)} e^{i\lambda z} d\lambda \to \frac{2\pi}{ik\left(d^2+y_0^2\right)^{1/2}} \frac{e^{-ikz}}{\ln\left(-\dfrac{2iz}{\Gamma^2 ka^2}\right)} \tag{58}$$

where $\Gamma = 1.781\cdots$. Substituting (58) in (57) and performing the derivative produces a second term that decays faster in z, so in the limit we are left with

$$I_D(z) \to \frac{\overline{I}_0 l y_0}{d^2+y_0^2} \frac{e^{-ikz}}{\ln\left(-\dfrac{2iz}{\Gamma^2 ka^2}\right)} \tag{59}$$

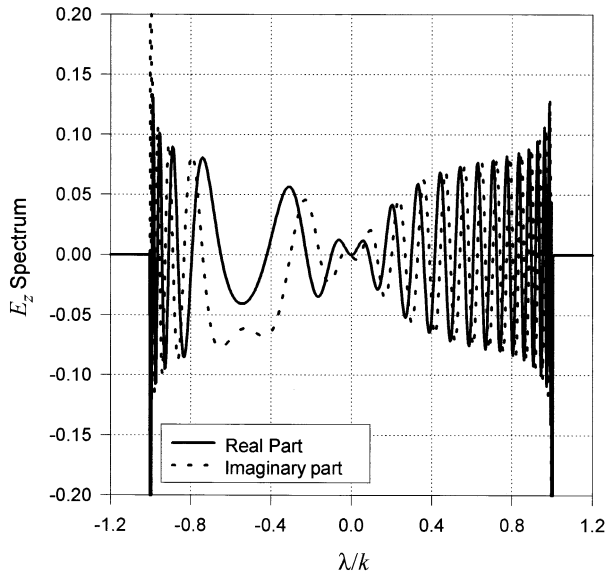

Figure 4. Amplitude of the integrand of the scattering integral for the continuous source case: $\beta/k = 1.1$, $d = 0.1$, $r = 10.0$, and $\theta = 1.0$ radians. Parameters d and r are given in wavelengths.

6. NUMERICAL RESULTS

The numerical integration techniques followed in calculating fields and currents are slightly different. In all plots that follow, we have set the operating wavelength λ_m and the excitation current I_0 to unity. We begin by examining the integrand of (21), where we notice that it is of oscillatory nature for all λ. For $|\lambda| > k$ the integrand is orders of magnitude smaller than for $|\lambda| < k$. The integrand does not increase without limit at the singularities at $\lambda = \pm k$ because of the Hankel functions in both numerator and denominator. However, the vicinity of these singularities introduces well-known numerical difficulties. Because of rapidly changing phase especially for large r, the frequency of oscillations rises as $\lambda \to \pm k$ from both sides, which makes numerical integration difficult (see Figure 4). The first step in performing numerical integration is to combine both sides of the integrand into one from 0 to infinity to reduce time of computation. Then to circumvent the problem of rapid oscillations near singularity we introduce the following mapping [22]

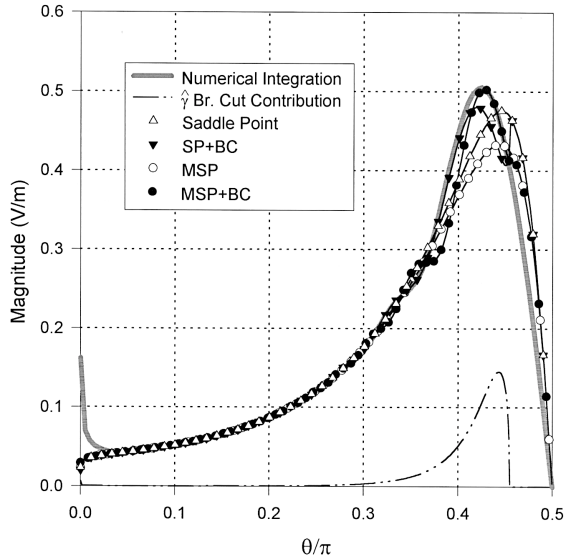

Figure 5. Magnitude of scattered field for the continuous source case: $\beta/k = 1.01$, $d = 0.5$, and $r = 10.0$; SP: Saddle point contribution; BC: Branch cut contribution; MSP: Modified SP contribution using parabolic cylinder functions.

$$\lambda = \begin{cases} k \sin \alpha, & 0 \le \lambda \le k \\ k \cosh\left(\alpha - \dfrac{\pi}{2}\right), & \lambda > k \end{cases}$$

This mapping spreads the oscillations more evenly and facilitates numerical integration. Since the integrand is on the real axis, it can be split into real and imaginary parts where zero crossings can be found analytically. We use a five-point Simpson's rule to integrate between zeros. The same argument is used for the scattering integral of the single dipole case. Because of the strong attenuation of the integrand for $\lambda > k$, it suffices to cut off the integration at $\lambda = 3k$. Analysis of the asymptotic behavior of the integrands from cutoff point to infinity has verified the validity of doing so. Figure 5 shows plots of standard and modified SP contributions with and without adding the contribution of branch cut (BC). Note that in the mid-range of θ the standard SP contribution follows closely the numerically integrated (NI) field, but deviates from it closer to broadside. Adding BC to SP adds the ripples missing in SP in the mid-range, and fixes part of the deviation from NI as can be seen just before $\theta = 0.4\pi$. The jump in SP and modi-

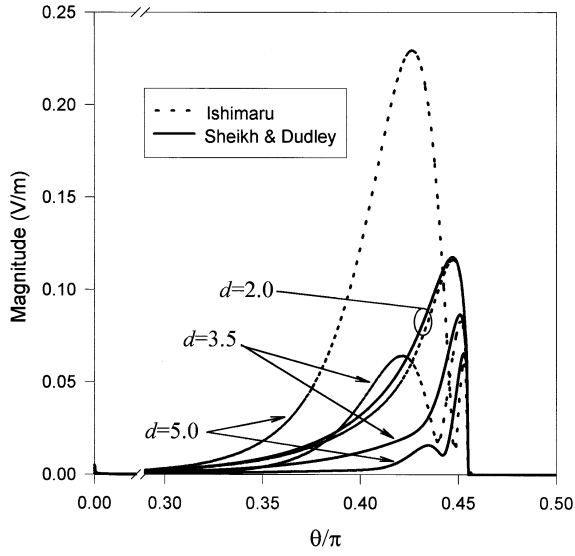

Figure 6. Behavior of the $\widehat{\gamma}$ branch cut integral approximation with increasing d: $\beta/k = 1.01$ and $r = 10.0$.

fied SP (MSP) around $\theta = 0.45\pi$ is a result of the assumption that the SP location and the SD path do not change when SP approaches branch point. The MSP provides a better performance than SP for $0.4\pi < \theta < 0.5\pi$ because it accommodates some effect of the BC. The approximation for the BC contribution we are using is the improved one (38). Although for the parameters shown in Figure 5 both Ishimaru's and the improved approximation give the same result, IA starts to give erroneous results for $d/\lambda_m > 1.5$, where λ_m is the operating wavelength in the surrounding medium (see Figure 6). As can be seen in Figures 7 and 8, all of these effects near broadside disappear when increasing β/k and/or kr. Near grazing, the asymptotic analysis cannot predict the existence of a singularity; however, this situation improves for larger r. Getting closer to grazing makes the observer closer to the scatterer, and makes the effect of traveling current far down the wire stronger than that near the center. This can be explained in Figure 9, where we show the fields produced from convolving current excited on the scatterer with the Green's function. The details of producing the field from current can be found in the Appendix A. We note that the SP contribution does not predict any oscillations in the field, and that convolving current extending on $z \in [-8, 8]$ gives better approxima-

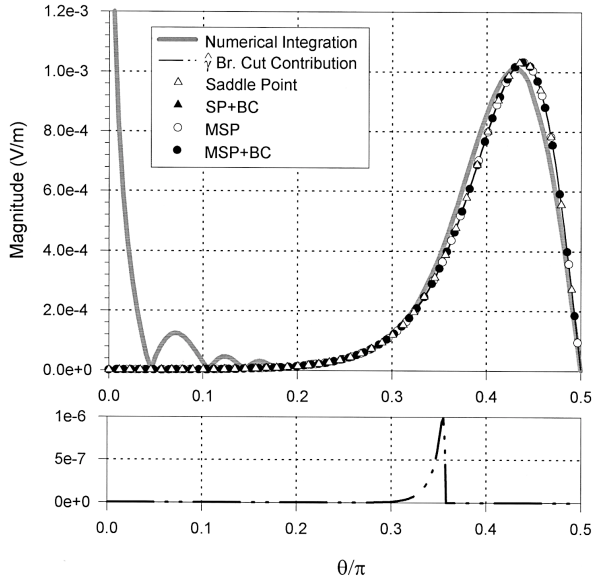

Figure 7. Magnitude of scattered field for the continuous source case: $\beta/k = 1.11$, $d = 1.9$, and $r = 10.0$.

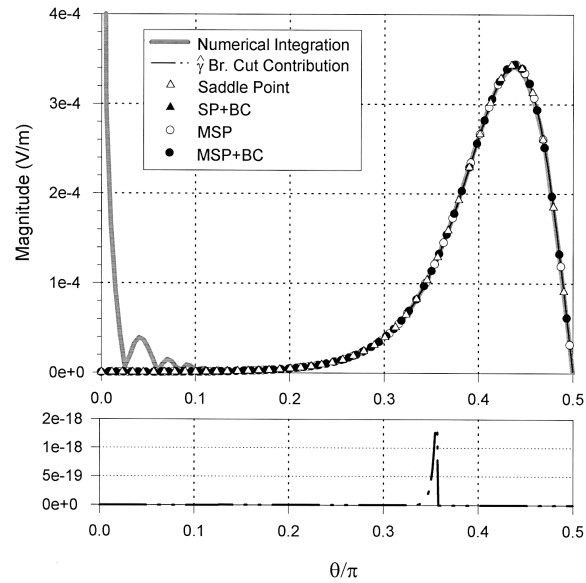

Figure 8. Magnitude of scattered field for the continuous source case: $\beta/k = 1.11$, $d = 1.9$, and $r = 30.0$.

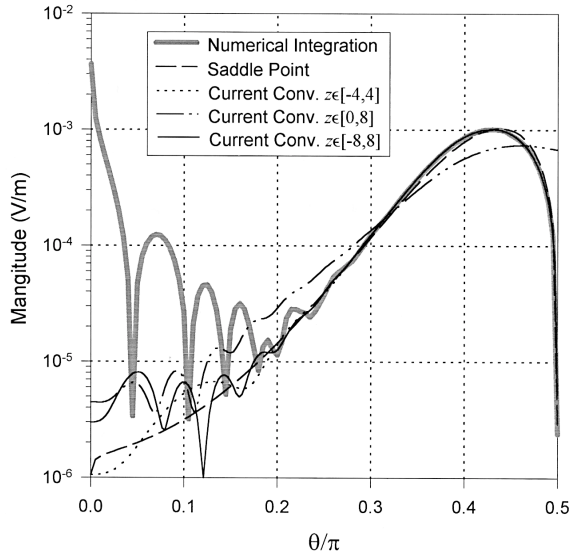

Figure 9. Comparison of scattered field produced from current convolution with that obtained numerically and by SD for the continuous source case: $\beta/k = 1.11$, $d = 1.9$, and $r = 10.0$.

tion to the field than that extending on $z \in [-4, 4]$. By this we mean that the field resulting from convolving the Hertzian dipole field with the portion of current excited on the scatterer from $z = -8$ to $z = 8$ is a better approximation to the numerically integrated field than that produced from the current on $z \in [-4, 4]$. However, the magnitude and frequency of field oscillations near grazing are affected only slightly by the current on the negative side of z as can be seen from convolving currents extending on $z \in [0, 8]$. This can be made clearer by visualizing the observer grazing the positive z-axis at $r = 10$. At such a position the observer is much closer to the current on the positive side of the z-axis than to the negative side. Of course at other values of θ, both positive and negative side currents are needed to produce the correct field.

In producing plots as shown in Figure 9, we use numerically computed currents from (22). In computing the current integral we did not produce asymptotic results for two reasons. First, the most important part of the current is that around the center of the scatterer in most of the cases. That is what produces most of the scattered field. Second, as is shown in current plots (Figure 10), the current

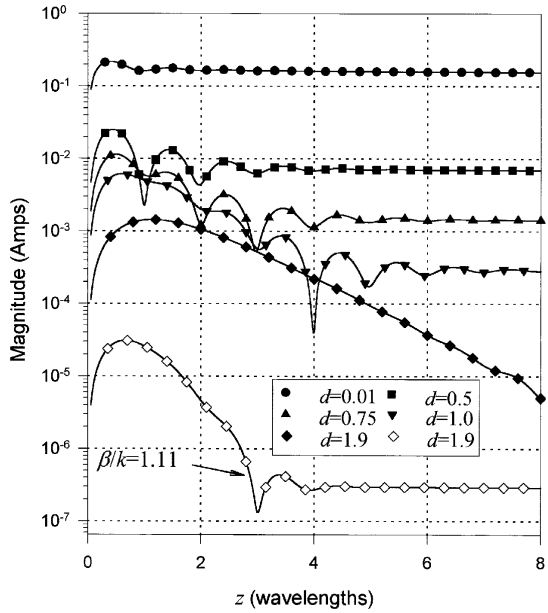

Figure 10. Magnitude of current excited on scatterer for the continuous source case: $\beta/k = 1.01$ except for the bottom curve, where $\beta/k = 1.11$.

quickly takes the form of traveling currents ($e^{-ik|z|}$) that are very slowly decaying. We expect this to happen because the current excited from a single dipole has the same behavior (59); we showed that superimposing dipole contributions approach that of the continuous source (see (52) to (55)). We return to the numerical integration of (22) to point out that the technique used here is slightly different than that used for calculating field integrals. This is because the nature of singularities in the integrand of (22) is different. At $\lambda = \pm k$ the integrand behaves as a logarithmic branch point (of $H_0^{(2)}(\gamma a)$) on top of a pole (from γ^2). This combination gives an overall singular behavior weaker than that of a pole. In addition, when performing the standard semi-circular contour integration around the singularity we get a residue of zero. We therefore perform the integration numerically in the complex plane on a contour that goes around the singularity. To evaluate the contribution from the singularity, we use a three-segment contour around $\lambda = \pm k$ (see $\mathrm{C_I}$ in Figure 2). Around $\lambda = +k$, the first segment starts from the origin at a $45°$ slope up to $\lambda = k + i\lambda_i$

where

$$\lambda_i = \begin{cases} 1, & |z| < 1 \\ 1/z, & |z| \geq 1 \end{cases}.$$

This is necessary to avoid growing exponentials in the integrand of (22) when $|z| \geq 1$. The second segment extends horizontally from $\lambda = k + i\lambda_i$ to $\lambda = \lambda_1 + i\lambda_i$, where λ_1 is the location of the first zero crossing of the integrand[2]. The third segment goes vertically down from $\lambda = \lambda_1 + i\lambda_i$ to $\lambda = \lambda_1$. On these segments the integrand is computed numerically, split into real and imaginary parts, then integrated using the quadrature routine DQAGS from the public domain SLATEC package [23]. For the rest of the real line integral ($\lambda > \lambda_1$) we use a combination of integration between zero crossings and asymptotic evaluation. By using asymptotic evaluation we save computation time. Details of evaluating the asymptotic integrand can be found in Appendix B. In order to verify the results obtained from the singularity contribution, we use another contour to go around it. The contour used here is a sine-shaped contour (see C_{II} in Figure 2) described parametrically in terms of $\mathrm{Re}(\lambda)$ and $\mathrm{Im}(\lambda)$. The reason for using such a contour instead of say, a semi-circle, is that we still can transform the integral into a semi-infinite one. Both contours produce the same result, but the three-segment contour is computationally faster by a factor of 1.5. In Figure 10 we show representative plots for the current on the scatterer for different distances from the source. Note that the current quickly takes the traveling form with the localized behavior becoming more apparent for $d/\lambda_m > 1$, and that increasing β/k accentuates localization. By localized we mean that current far down the scatterer is one or more orders of magnitude smaller than the current around the origin. It is in these cases that the oscillations appearing near grazing cannot be predicted by SD analysis, because the SP contribution is manifested physically from the current "bulge" around the center of scatterer. Since at grazing the observer is closer to the traveling current on the scatterer than to the "bulge", the field produced from traveling currents is more dominant than that produced from the central bulge. In Figure 11 we show representative plots for the excited scatterer current when the source is a single dipole. The

[2] In evaluating this integral we also use symmetry to transform the integral into a semi-infinite one. This results in a purely imaginary integrand for $\lambda > k$, which means that the only zero crossings are for this imaginary part.

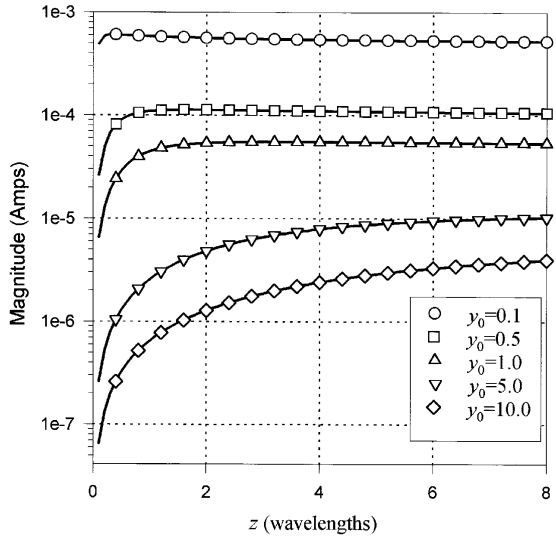

Figure 11. Magnitude of current excited on by a single dipole source: $\beta/k = 1.11$ and $d = 0.01$.

result exhibits traveling nature down the scatterer as predicted by (59). In Figure 12 we show that superimposing contributions from dipoles in a linear array approaches that of a continuous source. In order to show the converging behavior, it was very important to keep the distance between dipoles less or equal $0.01\lambda_m$.

We next summarize information about scattering effects from the scatterer perpendicular to the current source. We begin by showing a relief plot of the magnitude of the incident field from the continuous source for $\beta/k = 1.01$ (19) taken at the $y = 0$ plane (Figure 13). If this were a three dimensional plot of xyz coordinates, we would see the current source running vertically through the origin between the two peaks. We find two peaks because the incident field has a null at $z = 0$. Note that for a spherical coordinate system with the origin at $(x, y, z) = (0, 0, 0)$, the incident field has no symmetry with respect to any coordinate of (r, ϕ, θ) [3]. Note also that all the previously shown plots of scattered field were taken at a shifted coordinate system centered at $(x, y, z) = (d, 0, 0)$. This means that although the scattered

[3] It does have partial symmetry in θ. The field in $\theta\epsilon[0, \pi/2]$ is a mirror image to that in $\theta\epsilon[\pi/2, \pi]$ but opposite in sign.

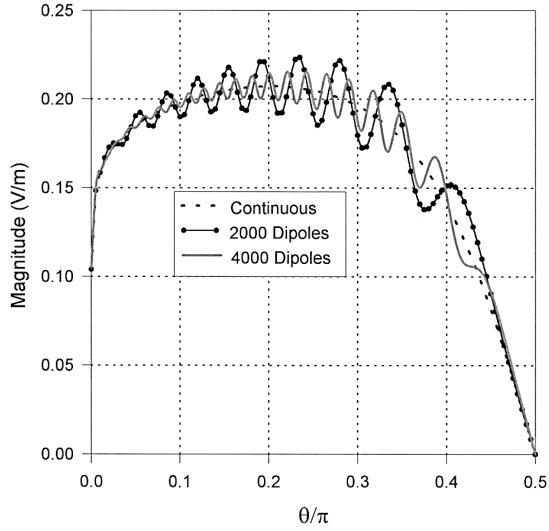

Figure 12. Magnitude of scattered electric field (SD approximation) for the cases of continuous and dipole array sources: $\beta/k = 1.11$, $d = 0.01$, $r = 50.0$, and $\Delta y_0 = 0.01$.

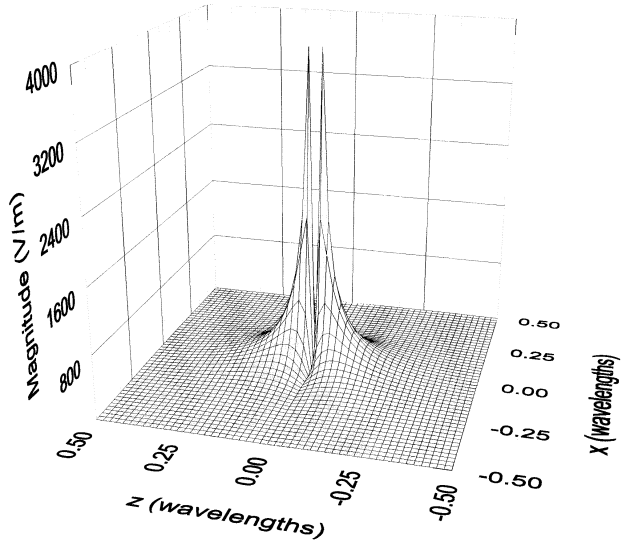

Figure 13. Magnitude of incident electric field for the continuous source case measured at $y = 0$ plane.

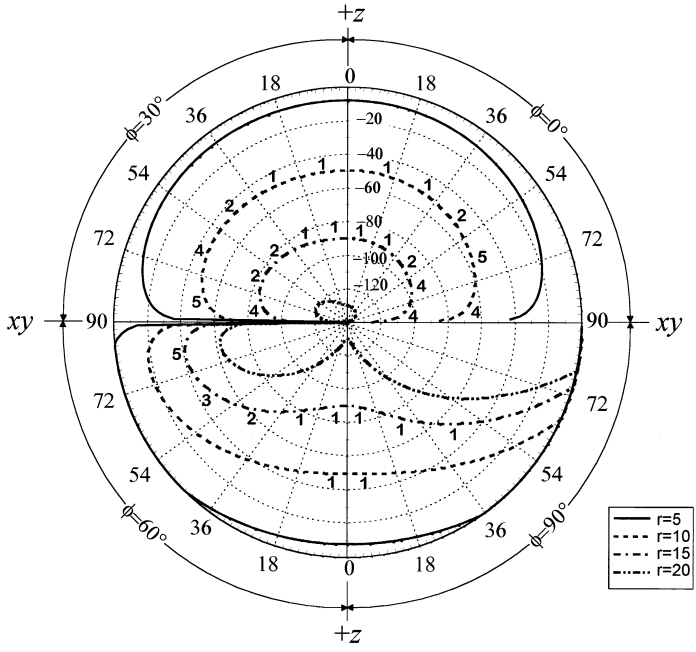

Figure 14. An example chart used to determine the minimum values of d for placing the scattering wire at selected angles if the total E_z field is not to exceed $-40\,\text{dbV}$: $\beta/k = 1.01$.

field is ϕ-independent in the shifted system, it is not in the original system. Our goal is to show scattering effects in the original coordinate system of the incident field.

Figure 14 contains plots of the incident field when $\beta/k = 1.01$ computed at four different values of ϕ, in this case: $\phi = 0°, 30°$, $60°$, and $90°$. The reason for choosing these values is that they also represent the field at other values. For example, the incident field has the same magnitude for the following groups of ϕ : $(0°, 180°)$, $(90°$, $270°)$, $(30°, 150°, 210°, 330°)$, and $(60°, 120°, 240°, 300°)$. The upper and lower halves of the vertical axis of the figure represents the $+z$ axis, while the horizontal axis represents the xy plane. Therefore θ can be read the usual way, from the $+z$ axis down to the xy plane. The numbers (0, 18, 36, 54, 72, and 90) are values of θ in degrees. We do not take θ further because the fields for $\theta \in [90°, 180°]$ are a mirror image of those for $\theta \in [0°, 90°]$. On each quadrant, there are four plots of the incident field computed at different values of r/λ_m. The

magnitude of the incident field is shown in db referred to 1 volt/meter (dbV). The concentric dotted circles represent different levels of dbV from -20 to -120, while the boundary of the chart is at 0 dbV. We can immediately see the strong attenuation of the incident field. For example, at $\phi = 0°$, increasing r by five wavelengths produce a magnitude dip of 40 dbV. Now suppose that we have an application that can be modeled by our continuous current source in free space. Suppose further that we need to place a perpendicular line conductor somewhere near the source such that at any given distance from $(x, y, z) = (0, 0, 0)$ we should have no more than -40 dbV total field. We orient the coordinate system so that the source is aligned on the y-axis, and the scatterer on the line described by $(x, y) = (d, 0)$. Assume that we are interested in measuring the level of electric field at $\phi = 0$. We examine the first quadrant of the figure. We discard measuring the field at $r/\lambda_m = 5$, because without the scatterer the incident field is more than -20 dbV. At $r/\lambda_m = 10$, however, the incident field is below -40 dbV. Note that at this value of ϕ, the scatterer is between the observer and the line current source. The numbers written on the $r/\lambda_m = 10$ curve indicate the *minimum* distance at which a scatterer can be placed without producing a total field exceeding -40 dbV. For example, if we are interested in levels of total field for the sector $\theta \in [0°, 36°]$, then we may place the scatterer at $d/\lambda_m \geq 1$. However, if we are interested in the sector $\theta \in [0°, 54°]$ then we must have the scatterer placed at $d/\lambda_m \geq 2$. The rest of the figure can be read in the same manner. The most important thing to remember is that although the observer's position changes for different (r, ϕ, θ), the scatterer's position is always on the $+x$ axis, d wavelengths from the origin. Sometimes at a certain distance only part of the curve meets our criterion of being below -40 dbV, in which case we limit our attention to only that part. For example, at $\phi = 60°$ and at $r/\lambda_m = 10$ we cannot look beyond $\theta = 18°$ because the incident field itself exceeds -40 dbV there. The figure serves as a concise and convenient means to examine many parameters of incident and scattered fields simultaneously without the need to consult many plots.

7. CONCLUSION

In this paper we have presented a full-wave analysis of the problem of scattering from an infinite thin wire excited by a perpendicular traveling current line source. We have presented results from standard

and modified asymptotic analysis as well as numerical integration of electric field and current integrals. We have shown that although the incident field is localized near the source, the scattered field is much wider spread. At distances well into the far zone, we have shown the standard steepest descent approximation to be in good agreement with numerical integration techniques. At moderate distances, however, a standard steepest descent analysis fails to give the correct fields close to broadside and close to grazing, with respect to the scatterer. We have explained the sources of the discrepancies and have produced improved results for some of them.

As future work, we plan to add another scatterer parallel to the first and on the other side of the line source. This structure will - in general - excite guided modes. We also plan to extend this into an array of scatterers on both sides, in which case Floquet's method might be used. Another extension might be to add dielectric cladding to the single or multiple scatterer cases, where guided modes will exist, even for the single scatterer. Finally, allowing β to be smaller than k will introduce totally different behaviors of both incident and scattered fields.

ACKNOWLEDGMENT

This problem was originally conceived ten years ago in a discussion between D. G. Dudley and A. C. Cangellaris concerning modelling certain aspects of high-speed interconnects. This present paper is an outgrowth of that discussion. The paper forms a part of the dissertation of M. M. Sheikh, submitted in partial satisfaction of the Ph.D. requirement at the University of Arizona. The authors are grateful to Professor S. L. Dvorak and the late Professor J. R. Wait for their useful discussions and deep insights regarding this paper and the related literature.

APPENDIX A.

Here we show how to produce the scattered electric field from currents excited on the wire. First, we show how to cast the scattered field as a convolution integral. Using operator notation, (21) can be written as

$$E_z^s = \mathcal{F}^{-1}\left[\mathrm{I}\left(\lambda\right)\mathrm{G}\left(\lambda\right)\right]$$

where

$$\mathrm{I}(\lambda) = 2I_0\beta \frac{\lambda e^{-id\widehat{\gamma}}}{\gamma^2 \widehat{\gamma} H_0^{(2)}(\gamma a)},$$

$$\mathrm{G}(\lambda) = -\frac{1}{4i\widehat{y}} \gamma^2 H_0^{(2)} \left\{ \gamma \left[(x-d)^2 + y^2 \right]^{1/2} \right\}, \text{ and}$$

$$\mathcal{F}^{-1}[\cdot] = \frac{1}{2\pi} \int_{-\infty}^{\infty} (\cdot)\, e^{i\lambda z} d\lambda.$$

This means that

$$\begin{aligned} E_z^s &= I(z) \otimes G(z) \\ &= \int_{-\infty}^{\infty} I(\xi)\, G(z-\xi)\, d\xi \end{aligned}$$

where $I(z)$ and $G(z)$ are the inverse Fourier transforms of $\mathrm{I}(\lambda)$ and $\mathrm{G}(\lambda)$ respectively. A careful examination of $G(z)$ reveals that it is the field generated by a Hertzian dipole (see for example [13, eq. 2–113]). To arrive at the familiar form for the radiation of a Hertzian dipole that involves exponentials, we use a well known Hankel function identity [12, eq. 4.306]. Now that we have established the field as a convolution, we have to use numerical techniques since $I(z)$ is only available as data around the center of the scatterer. We use a very simple algorithm that represents the following formula

$$E_z^s(x,y,z) = \Delta_{z'} \sum_{j=1}^{N} I(z_j') G(x,y,z-z_j'), \text{ where}$$

$$\Delta_{z'} = z_2' - z_1',$$

and N is the number of data points in $I(z)$. Note that in the above formula, each set of N points of G has the correct (x,y,z) dependence.

APPENDIX B.

Here we show how to develop the expressions for the current integral for large $|\lambda|$. Referring to (22), we use symmetry and the fact that $\widehat{\gamma}$ is pure imaginary to reduce the domain of integration, viz:

$$I(z) = -\frac{2I_0\beta}{\pi} \int_0^{\infty} \frac{\lambda e^{-d\widetilde{\gamma}}}{\gamma^2 \widetilde{\gamma} H_0^{(2)}(\gamma a)} \sin(\lambda z) d\lambda,$$

where $\widetilde{\gamma} = i\widehat{\gamma}$ is real. We now focus our attention on evaluating the integral for $|\lambda| \gg k$ where γ becomes imaginary. We split the above integral into two parts, one evaluated numerically from 0 to λ_c and the other evaluated asymptotically from λ_c to ∞, where λ_c is a cutoff value after which asymptotic approximations are valid. In this region we assume that $\widetilde{\gamma} \to \lambda, \gamma \to -i\lambda$, and $H_0^{(2)}(\gamma a) \to (2i/\pi)K_0(\lambda a) \to (2i/\pi)\exp(-\lambda a)/(2\lambda a/\pi)^{1/2}$. Hence the asymptotic integral becomes

$$I_c(z) = i\left(\frac{\pi a}{2}\right)^{1/2} \mathrm{Im}\left(\int_{\lambda_c}^{\infty} \lambda^{-3/2} e^{-\lambda(d-a)} e^{i\lambda z} d\lambda\right). \tag{60}$$

Let us denote the integral inside the parentheses above by $\overline{I}_c$ and let us perform a change of variables, viz:

$$\overline{I}_c = \lambda_c^{-1/2} \int_1^{\infty} t^{-3/2} e^{-\zeta t} dt, \text{ where}$$
$$\zeta = \lambda_c (d - a - iz).$$

The above integral can be expressed in terms of the confluent hypergeometric function defined in [16, eq. 13.2.6] as follows

$$U(a, b; \zeta) = \frac{1}{\Gamma(a)} e^{\zeta} \int_1^{\infty} e^{-\zeta t} (t-1)^{a-1} t^{b-a-1} dt,$$
$$\text{where } \mathrm{Re}(a) > 0, \quad \mathrm{Re}(\zeta) > 0.$$

Thus $\overline{I}_c$ becomes

$$\overline{I}_c = \lambda_c^{-1/2} e^{-\zeta} U(1, \frac{1}{2}; \zeta).$$

We have developed an efficient algorithm to compute U in much shorter time compared to numerical integration.

REFERENCES

1. Olsen, R. G., and M. A. Usta, "The excitation of current on an infinite horizontal wire above earth by a vertical electric dipole," *IEEE Trans. Antennnas Propagat.,* Vol. AP-25, 560–565, Jul. 1977.
2. Hill, D. A., and J. R. Wait, "Coupling between a dipole antenna and an infinite cable over an ideal ground plane," *Radio Sci.,* Vol. 12, No. 2, 231–238, March–April 1977.

3. Wait, J. R., "Excitation of a coaxial cable or wire conductor located over the ground by a dipole radiator," *Archiv Elektronik Uber.,* Vol. 31, No. 3, 121–127, 1977.
4. Wait, J. R., "Excitation of an ensemble of parallel cables by an external dipole over a layered ground," *AEU,* Vol. 31, No. 12, 489–493, 1977.
5. Giri, D. V., S. Chang, and F. M. Tesche, "A coupling model for a pair of skewed transmission lines," *IEEE Trans. Electromag. Compat.,* Vol. EMC-22, No. 1, 20–28, Feb. 1980.
6. Kami, Y., and R. Sato, "Coupling model of crossing transmission lines," *IEEE Trans. Electromag. Compat.,* Vol. EMC-28, No. 4, 204–210, Nov. 1986.
7. Uwano, T., R. Sorrentino, and T. Itoh, "Characterization of strip line crossing by transverse resonance analysis," *IEEE Trans. Microwave Theory Tech.,* Vol. MTT-35, No. 12, 1369–1376, Dec. 1987.
8. Papatheodorou, S., R. F. Harrington, and J. R. Mautz, "The equivalent circuit of a microstrip crossover in a dielectric saubstrate," *IEEE Trans. Microwave Theory Tech.,* Vol. 38, No. 2, 135–140, Feb. 1990.
9. Young, J. L., "TEM coupling between orthogonal crossing wires: A closed-form approximation," *IEEE Trans. Microwave Theory Tech.,* Vol. MTT-42, 884–890, May 1994.
10. Wait, J. R., "Interaction of a vertical line current with a horizontal cable over a perfectly conducting plane," *IEEE Trans. Electromag. Compat.,* Vol. 38, 605–607, Nov. 1996.
11. Wait, J. R., "EM fields of a phased line current over a conducting half-space," *IEEE Trans. Electromag. Compat.,* Vol. 38, No. 4, 608–611, Nov. 1996.
12. Dudley, D. G., *Mathematical Foundations for Electromagnetic Theory,* IEEE Press, 1st edition, New York, 1994.
13. Harrington, R. F., *Time-Harmonic Electromagnetic Fields,* 1st edition, McGraw-Hill Inc., New York, 1961.
14. Sheikh, M. M., *Scattering from a Thin Wire Excited by a Perpendicular Line Current Source,* Ph.D. thesis, University of Arizona, 1998.
15. Felsen, L. B., and N. Marcuvitz, *Radiation and Scattering of Waves,* 1st edition, Prentice-Hall, Englewood Cliffs, 1973.
16. Abramowitz, M., and I. A. Stegun, *Handbook of Mathematical Functions,* Dover edition, Dover, New York, 1972.
17. Ishimaru, A., *Electromagnetic Wave Propagation, Radiation, and Scattering,* 1st edition, Prentice-Hall, Englewood Cliffs, 1991.

18. Bleistein, N., "Uniform asymptotic expansions of integrals with stationary point near algebraic singularity," *Comm. Pure Appl. Math.,* Vol. 19, No. 4, 353–370, 1966.
19. Whittaker, E. T., and G. N. Watson, *A Course of Modern Analysis,* 4th edition, Cambridge Univ. Press, London, 1962.
20. Kunz, K. S., "Asymptotic behavior of the current on an infinite cylindrical antenna," *J. Res. NBS Sec D. (Radio Propagation),* Vol. 67D, No. 4, 417–431, July/Aug. 1963.
21. Wait, J. R., and D. A. Hill, "Theory of transmission of electromagnetic waves along a drill rod in conducting rod," *IEEE Trans. Geos. Electronics,* Vol. GE-17, No. 2, 21–24, Apr. 1979.
22. Johnson, W. A., and D. G. Dudley, "Real axis integration of sommerfeld integrals: Source and observation points in air," *Radio Sci.,* Vol. 18, No. 2, 175–186, March–April, 1983.
23. "SLATEC Common Math Library," Distributed by The Energy Science and Technology Software Center, PO Box 1020, Oak Ridge, TN 37831, Version 4.1, 1993, also obtainable from http://www.netlib.org/slatec/src/.